Korean J. Chem. Eng., 34(8), 2331-2341 (2017)
DOI: 10.1007/s11814-017-0135-9

pISSN: 0256-1115
eISSN: 1975-7220

Preparation and photocatalytic activity of composite metal oxides derived from Salen-Cu(II) intercalated layered double hydroxides

Yue Meng[*,], Shengjie Xia[*], Guoxiang Pan[***], Jilong Xue[*], Junhui Jiang[*], and Zheming Ni[*,†]**

*College of Chemical Engineering, Zhejiang University of Technology, Hangzhou 310014, China
**School of Life Sciences, Huzhou University, Huzhou 313000, China
***School of Engineering, Huzhou University, Huzhou 313000, China
(*Received 17 January 2017 • accepted 17 May 2017*)

Abstract−Copper(II) Schiff-base Complexes (Salen-Cu(II)) intercalated zinc-chromium layered double hydroxides (ZnSBCuCr-LDHs) were successfully prepared via coprecipitation. Then, a novel photocatalytic material Zn-Cu-Cr composite oxides (ZnSBCuCr-MO) was prepared after calcination at 500 °C with ZnSBCuCr-LDHs as precursor. The structure and properties of the materials were thoroughly characterized by powder X-ray diffraction (XRD), inductively coupled plasma atomic emission spectrometry (ICP-AES), ultraviolet visible diffuse reflectance spectroscopy (UV-Vis DRS), scanning electron microscopy (SEM) and X-ray photoelectron spectroscopy (XPS). The photocatalytic activities of the materials were investigated by photodegradation of a cationic dye Rhodamin B (RhB), which was hard to adsorb by LDHs. The effects of the photocatalyst dosage, the initial pH and temperature of RhB solution on the photocatalytic efficiency were discussed. The results showed that ZnSBCuCr-MO displayed higher photocatalytic activity for RhB than calcined ZnCr-LDHs (ZnCr-MO) and calcined ZnCuCr-LDHs (ZnCuCr-MO). Meanwhile, ZnSBCuCr-MO exhibited better stability and reusability. In addition, the possible photocatalytic mechanism and degradation pathway for RhB were studied through density functional theory (DFT) calculation of the RhB molecule, UV-vis absorption variation and LC-MS analyses of the RhB solution.

Keywords: Salen-Cu (II), Layered Double Hydroxides, Composite Metal Oxides, Rhodamin B, Photodegradation Mechanism

INTRODUCTION

Layered double hydroxides (LDHs), a class of anionic clay materials, consist of a flat 2-D network composed of unique octahedral layer structure. The general formula of these materials is as $[M^{2+}_{1-x}M^{3+}_{x}(OH)_2]^{x+}(A^{n-})_{x/n}\cdot mH_2O$, where M^{2+} and M^{3+} are divalent mental cations and trivalent mental cations in the host layer, respectively, and A^{n-} are any exchangeable inorganic or organic anions in the gallery between the host layers [1-4]. Because of the anion-exchange ability of the A^{n-}, different guest anions can be exchanged with A^{n-} into the LDHs interlayer. Then, a series of special functional materials with both the main features of LDHs and the characteristics of intercalated anions will be obtained [5-9]. These materials have been applied in catalysis, adsorption, photocatalysis, magnetics, electrochemistry, medicine and environment, and so on. If they are further calcined, composite metal oxides as photocatalytic materials can be obtained. For photocatalytic materials, traditional TiO_2 based materials are well known based on their good properties such as well resourced, photostability and powerful oxidation ability [10]. But, in the practical application, they still have some problems like only response in UV region, low quantum yield, hard floating and difficult for recycling [11,12]. However, the calcined LDHs can overcome these disadvantages. They have higher specific surface area, higher pore volume, better pore size distribution, and narrower bandgap showing better photocatalytic activities in the visible region [13,14].

Metallorganic compound intercalated LDHs are new a kind of functional intercalated materials. The guest complexes anions and the host LDHs are both arranged in an orderly manner through the interaction of ionic bond, hydrogen bond and van der Waals force, becoming a class of organic-inorganic hybrid composites with supramolecular structure [15-18]. Then, after the metallorganic compound intercalated LDHs are calcined, a novel type of composite metal oxides can be obtained. These materials may have more uniform metal distribution, higher metal content, stronger stability, and better activity than other materials containing similar ingredients, such as traditional calcined LDHs [19]. RhB, a cationic xanthene dye, is a typical pollutant in dye wastewater which is toxic and difficult to degrade. The photocatalytic technology can overcome the problem of difficult treatment of cationic pollutants over LDHs-based materials. It has the advantages of high efficiency, thorough degradation level and no secondary pollution. In the previous work, we introduced the metal titanium organic complexes into the LDHs interlayer, and then obtained novel composite metal oxides with small size uniformity, structural stability, and excellent photocatalytic performance after high temperature calcination [20]. The novel composite metal oxides mentioned above are likely to be effective photocatalysts for degradation of RhB.

†To whom correspondence should be addressed.
E-mail: nzm@zjut.edu.cn

Based on the above ideas, in this study, for the first time, Salen-Cu (II) as a copper source was intercalated into the ZnCr-LDHs interlayer by coprecipitation method. Then a novel photocatalytic material (abbreviated as ZnSBCuCr-MO) with excellent physical and chemical properties was obtained after calcination at high temperature. The photocatalytic activity of ZnSBCuCr-MO was investigated by using cationic dye RhB as the model pollutant under simulated visible light, and compared with calcined ZnCr-LDHs (abbreviated as ZnCr-MO) and calcined ZnCuCr-LDHs (abbreviated as ZnCuCr-MO). The influences of various operational parameters (catalyst dosage, pH, reaction temperature) on photocatalytic degradation were systematically investigated. In addition, the path and mechanism of photocatalytic degradation of RhB were investigated by the analysis of the frontier electron densities (FEDs) on atoms of RhB from DFT calculation, the UV-vis absorption variation analysis of the RhB solution, and the LC-MS analysis of the intermediate degradation products.

MATERIALS AND METHODS

1. Materials

All the reagents were analytical grade (AR) and used without further purification. RhB, *p*-aminobenzoic acid and salicylaldehyde were purchased from Aladdin Chemistry Co. Ltd. The other reagents were all purchased from Sinopharm Chemical Reagent Co. Ltd. Deionized water decarbonated by boiling and bubbling N_2 was used throughout all synthesis steps.

2. Preparation of the Materials

2-1. Preparation of Salen-Cu (II) Complex

In a 250 ml three-necked flask, 6.85 g (50 mmol) p-aminobenzoic acid was dissolved in 100 ml absolute ethanol by magnetic stirring. 6.10 g (50 mmol) salicylaldehyde dissolved in 40 ml absolute ethanol was slowly added dropwise to the ethanol solution of p-aminobenzoic acid. After the dropwise addition, the reaction system was heated to reflux for 3 h with continuous stirring. Then the resultant slurry was cooled, filtered, washed and dried at 65 °C for 24 h to obtain a bright yellow needle-like Salen, marked as SBH. After that, under magnetic stirring, 25 mL ethanol containing 0.24 g (6 mmol) NaOH was added dropwise to the 100 mL absolute ethanol containing 1.45 g (6 mmol) SBH and stirred at room temperature for 30 min. Then, 10 ml deionized water containing 0.75 g (3 mmol) $CuSO_4 \cdot 5H_2O$ was added dropwise to the above solution and slowly appeared green turbidity. After dropwise addition, the greenish turbid solution was heated to reflux for 3 h. Finally, the slurry was cooled, filtered, washed, dried at 65 °C for 24 h to get dark green Salen-Cu(II), marked as SBCu (Scheme 1).

2-2. Preparation of ZnSBCuCr-MO

First, Salen-Cu(II) intercalated ZnCr-LDHs were synthesized by coprecipitation under nitrogen atmosphere. The synthesis process was as follows: an aqueous solution of NaOH (1 M) and a mixed solution (60 mL) containing 6.25 g $Zn(NO_3)_2 \cdot 6H_2O$, 2.80 g $Cr(NO_3)_3 \cdot 9H_2O$ (initial Zn : Cr=3 : 1) were simultaneously added dropwise to a solution (30 mL) containing 4.13 g Salen-Cu(II) (initial Cu : Cr= 1 : 1) with vigorous stirring at room temperature until the final pH

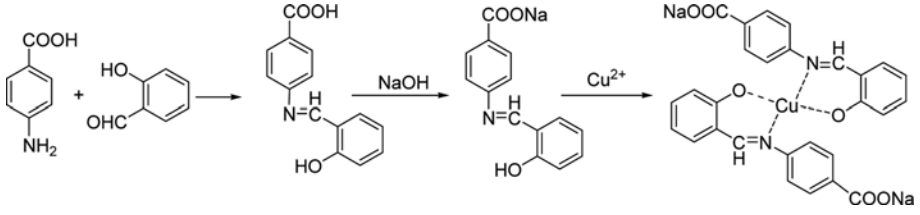

Scheme 1. The preparation pathway of the SBCu.

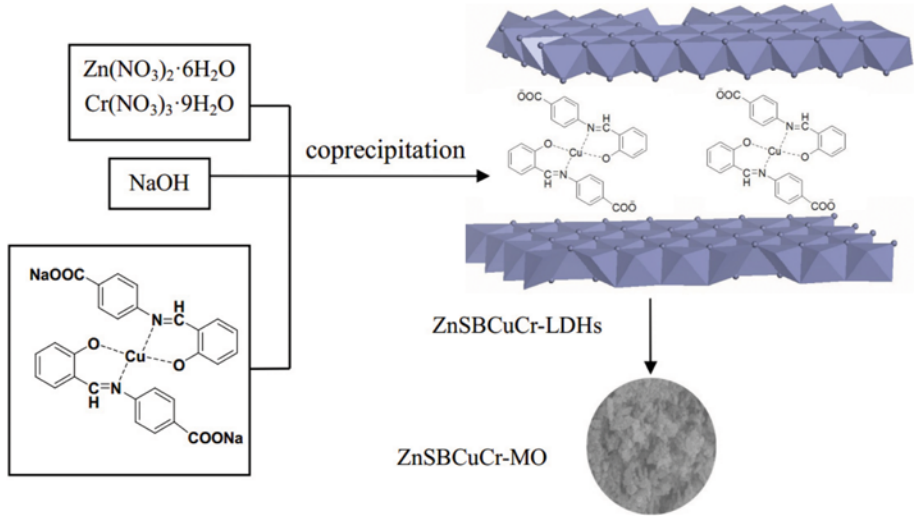

Scheme 2. The preparation pathway of the ZnSBCuCr-MO.

at 9.5-10. Then, the reaction system was stirred for 12 h under N_2 atmosphere and aged at 85 °C for 18 h. Finally, the resulting slurry was centrifuged, washed to neutral, dried at 65 °C for 24 h, and ground, obtaining Salen-Cu(II) intercalated ZnCr-LDHs, marked as ZnSBCuCr-LDHs. And then, the as-prepared ZnSBCuCr-LDHs was calcined in a muffle furnace at 500 °C for 4 h to obtain composite metal oxides, marked as ZnSBCuCr-MO. The complete preparation pathway of the ZnSBCuCr-MO is shown in Scheme 2.

2-3. Preparation of ZnCr-MO and ZnCuCr-MO

First, ZnCr-LDHs and ZnCuCr-LDHs were prepared through the coprecipitation method under nitrogen atmosphere. The preparation procedure was as follows: solution A, the metal nitrate solution with certain molar ratio, was prepared by dissolving $Zn(NO_3)_2 \cdot 6H_2O$, $Cr(NO_3)_3 \cdot 9H_2O$/$Zn(NO_3)_2 \cdot 6H_2O$, $Cu(NO_3)_2 \cdot 6H_2O$, $Cr(NO_3)_3 \cdot 9H_2O$ (Zn : Cr=3 : 1/Zn : Cu : Cr=3 : 1 : 1). Solution B (1 M), the alkali solution, was prepared by dissolving NaOH in deionized water. Solution A and solution B were slowly added simultaneously into the deionized water. The pH of the reaction system was maintained 9.5-10, stirred for 45 minutes and aged at 85 °C for 18 h. The resulting slurry was centrifuged, washed to neutral, dried at 65 °C for 24 h, and ground, obtaining ZnCr-LDHs/ZnCuCr-LDHs. Finally, the as-prepared ZnCr-LDHs/ZnCuCr-LDHs were calcined at 500 °C for 4 h to obtain composite metal oxides, marked as ZnCr-MO/ZnCuCr-MO.

3. Materials Characterization

Powder X-ray diffraction (PXRD) data of prepared materials were collected on Beijing Puxi XRD-6 type diffractometer using Cu Ka radiation (λ=0.15418 nm) at 6 kV, 20 mA and the scanning rate was 4°/min in the region of 2θ from 5° to 70°. The metallic elements compositions of the materials were determined by inductively coupled plasma atomic emission spectrometry (ICP-AES) on an IRIS Intrepid II XSP instrument. The surface morphologies of the materials were characterized by Hitachi S-4700 scanning electron microscope (SEM, acceleration voltage 15 kV), and the elemental composition of the material was analyzed by X-ray energy dispersive spectroscopy (EDS). The UV-Vis diffuse reflectance spectra (UV-Vis DRS) were measured by Shimadzu-2550 UV-Vis spectrophotometer with an integrating sphere attachment using $BaSO_4$ as background at room temperature in air.

4. Photocatalytic Reaction

The photocatalytic activity of the materials was tested by degradation of RhB as a model reaction with simulated visible light using a 300 W Xenon lamp (380 nm<λ<760 nm, light source is 25 cm from the reaction solution). Briefly, a certain amount of catalytic material was added to a double-layer quartz reaction tube containing 50 mL of 5 mg/L RhB solution at a certain temperature and pH. First, the adsorption-desorption equilibrium of RhB was achieved by stirring for 30 min in the dark. Then, the xenon lamp was turned on and the photocatalysis experiment was carried out under continuous illumination and magnetic stirring. After the start of the reaction, 2 ml aliquots were sampled every 1 h and the absorbance at 554 nm was measured by UV-visible spectrophotometer (Shimadzu-2550) after filtration through a filter membrane, and then converted into the relative mass concentration of RhB. The degradation efficiency of RhB was calculated according to C/C_0, and C_0 (mg/L) was the relative mass concentration of RhB after the adsorption-desorption equilibrium. Degradation products in RhB solution after a certain period of light exposure were determined by a Waters 2695 high performance liquid chromatograph equipped with a Therm LCQ (TM) Deca XP plus ion trap mass spectrometer (LC-MS).

RESULTS AND DISCUSSION

1. Characterization of the Materials

Fig. 1 shows the XRD diffraction pattern of LDHs (ZnCr-LDHs, ZnCuCr-LDHs and ZnSBCuCr-LDHs) and their composite metal oxides (ZnCr-MO, ZnCuCr-MO and ZnSBCuCr-MO). In Fig. 1(A), all of the materials show the reflections of (003), (006), (009), which can be indexed to typical LDHs materials [21]. The (003) lattice diffraction peak of ZnCr-LDHs appears at 2θ=9.99°. While the (003) lattice diffraction peak of ZnSBCuCr-LDHs appears at a lower angle of 2θ=7.77°, which shows that the interlayer spacing of ZnSBCuCr-LDHs becomes 1.14 nm. Subtracting the thickness

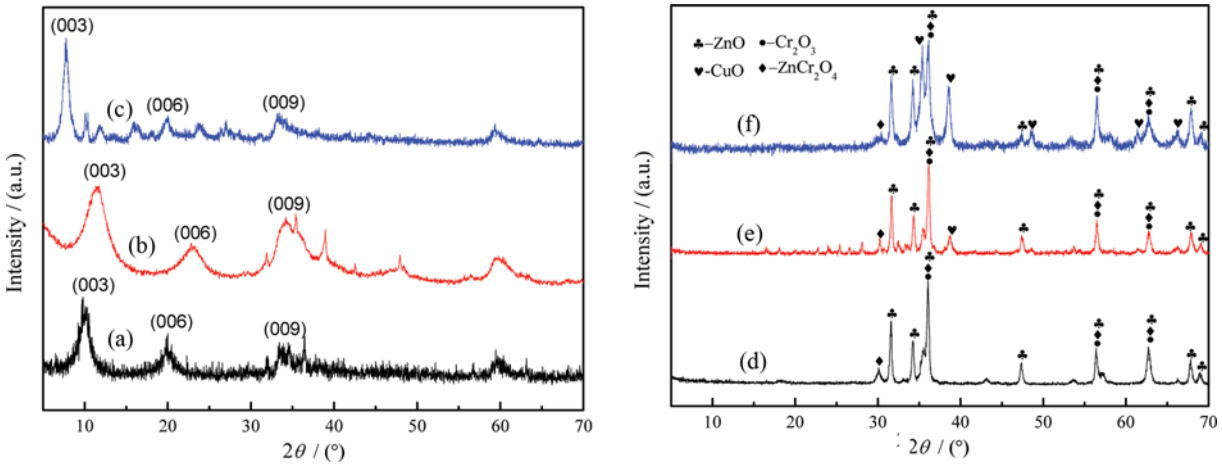

Fig. 1. XRD patterns of materials: (A) ZnCr-LDHs (a), ZnCuCr-LDHs (b), ZnSBCuCr-LDHs (c); (B) ZnCr-MO (d), ZnCuCr-MO (e), ZnSB-CuCr-MO (f).

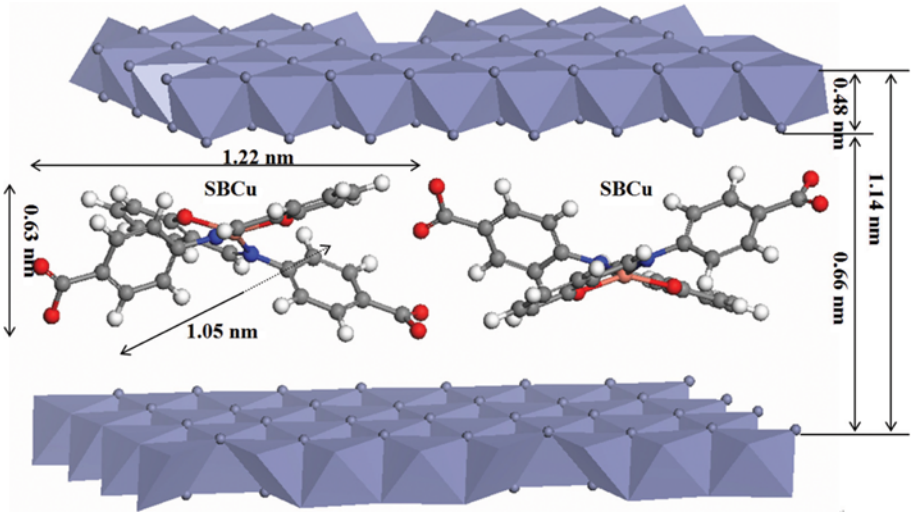

Fig. 2. The schematic illustration of ZnSBCuCr-LDHs.

of the LDHs plate (0.48 nm), the gallery height of ZnSBCuCr-LDHs is 0.66 nm (1.14-0.48=0.66 nm). Fig. 2(B) shows that after calcination at 500 °C, the characteristic diffraction peaks of LDHs at (003), (006) and (009) disappear. It indicates that the LDHs lamellae collapse and the lamellar structure is destroyed forming composite metal oxides. The characteristic diffraction peaks of ZnO (JCPDS NO. 36-1451), spinel $ZnCr_2O_4$ (JCPDS NO. 22-1107) and Cr_2O_3 (JCPDS NO. 38-1479) are observed in all of the composite metal oxides. In addition, for ZnSBCuCr-MO (Fig. 1(B f)), the characteristic diffraction peaks of hexagonal CuO (JCPDS NO. 45-0937) are more obvious than ZnCuCr-MO (Fig. 1(B e)). CuO is a kind of narrow band-gap semiconductor; it may further promote the separation of photo-generated electrons and holes.

From the above results, it is known that the gallery height of ZnSBCuCr-LDHs is 0.66 nm, which is higher than that of ZnCr-LDHs. To further investigate the intercalation of ZnSBCuCr-LDHs, we used Materials Studio 5.5 software to simulate SBCu molecule. The calculated size of SBCu was 1.22 nm×1.05 nm×0.63 nm. Therefore, it is inferred that the anion of this complex is arranged perpendicularly to the laminates in the shortest dimension between the LDHs laminates, as shown in Fig. 2.

ICP-AES analyses were performed to further investigate the amount of Salen-Cu(II) containing in LDHs and the metallic composition of the composite metal oxides. As presented in Table 1, the actual molar ratio of Zn : Cu : Cr in ZnSBCuCr-LDHs is close to the prospective molar ratio and after calcination at 500 °C the molar ratio of Zn : Cu : Cr is essentially remained. In addition, the molar ratios of metallic elements in ZnCr-MO and ZnCuCr-MO are also close to the prospective mole ratios.

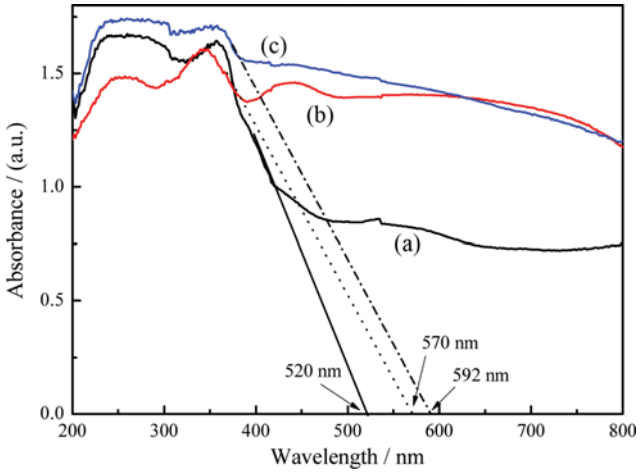

Fig. 3. UV-vis diffuse reflectance spectra of the materials (a) ZnCr-MO; (b) ZnCuCr-MO; (c) ZnSBCuCr-MO).

The UV-Vis diffuse reflectance spectra of ZnCr-MO, ZnCuCr-MO and ZnSBCuCr-MO are shown in Fig. 3. All the materials were visible-light-responsive. As shown in Fig. 3, the absorption edge (λ) of ZnCr-MO, ZnCuCr-MO and ZnSBCuCr-MO was 520 nm, 570 nm and 592 nm, respectively. So, based on the formula of $E_g = 1240/\lambda$ (nm) [22], where λ is the wavelength corresponding to the absorption onset, the optical band gap energies of the materials are 2.38 ev, 2.18 ev and 2.09 ev, respectively. Thus, compared with ZnCr-

Table 1. The metallic composition of the materials

Materials	Zn (ppm)	Cu (ppm)	Cr (ppm)	Actual molar ratio (Zn : Cr/Zn : Cu : Cr)	Prospective molar ratio (Zn : Cr/Zn : Cu : Cr)
ZnSBCuCr-LDHs	11.71	3.58	3.07	3.05 : 0.95 : 1	3 : 1 : 1
ZnSBCuCr-MO	16.90	4.87	4.12	3.09 : 0.96 : 1	3 : 1 : 1
ZnCr-MO	23.62	-	6.22	3.04 : 1	3 : 1
ZnCuCr-MO	19.31	6.56	5.11	3.02 : 1.02 : 1	3 : 1 : 1

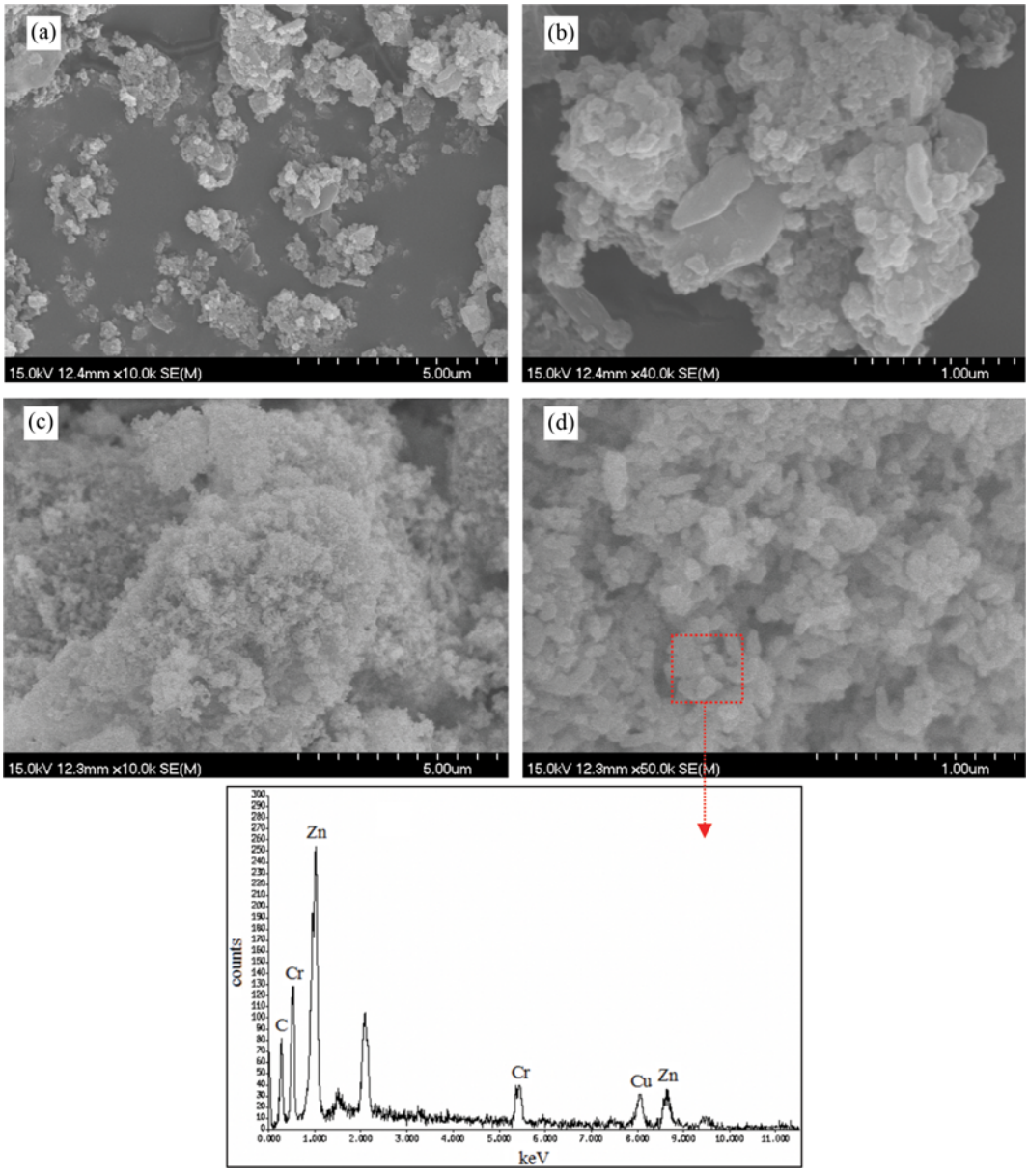

Fig. 4. SEM images for ZnSBCuCr-LDHs with low-(a) and high-magnification (b); ZnSBCuCr-MO with low-(c) and high-magnification (d); the EDS analysis of designated area (e) of ZnSBCuCr-MO.

MO and ZnCuCr-MO, ZnSBCuCr-MO with the narrowest band gap requires the least energy to excite electrons. Therefore, ZnSBCuCr-MO is more conducive to photoelectron-hole separation to produce more free electrons, which effectively improves the photocatalytic process effectiveness [23,24], indicating that ZnSBCuCr-MO may be a potential better photocatalytic material.

The morphologies of ZnSBCuCr-LDHs and ZnSBCuCr-MO were investigated by SEM (coupled with EDS). In Fig. 4(a), (b), ZnSBCuCr-LDHs is typical layered lamellar-shaped morphology and the dense regions are laminated to each other, confirming the formation of LDHs material. The SEM images of ZnSBCuCr-MO (Fig. 4(c), (d)) show that the layered structure of ZnSBCuCr-LDHs has disappeared after being calcined at 500 °C, and many small particles appear. In addition, the EDS result in Fig. 4(e) shows that ZnSBCuCr-MO contains Zn, Cu and Cr as main metal components.

The chemical states of Zn, Cu, and Cr in ZnSBCuCr-MO before and after photocatalytic degradation were determined by X-ray photo-electron spectroscopy (XPS). To avoid error in peak shifts, the binding energy for C 1 speak at 284.6 eV was used as the reference for calibration of all peaks. The high resolution spectra of Zn2p, Cu2p, and Cr2p for the material before photocatalytic degradation are presented in Fig. 5(A-a), Fig. 5(B-a), and Fig. 5(C-a), respectively. As shown in Fig. 5(A-a), the binding energies of 1,021.6 eV and 1,044.5 eV are ascribed to Zn 2p3/2 and Zn 2p1/2. The difference of 22.9 eV in Zn 2p3/2 and Zn 2p1/2 levels indicates an oxidation state of 2+ for the Zn element [25]. As shown in Fig. 5(B-a), the binding energies of 993.4 eV and 955.9 eV are ascribed

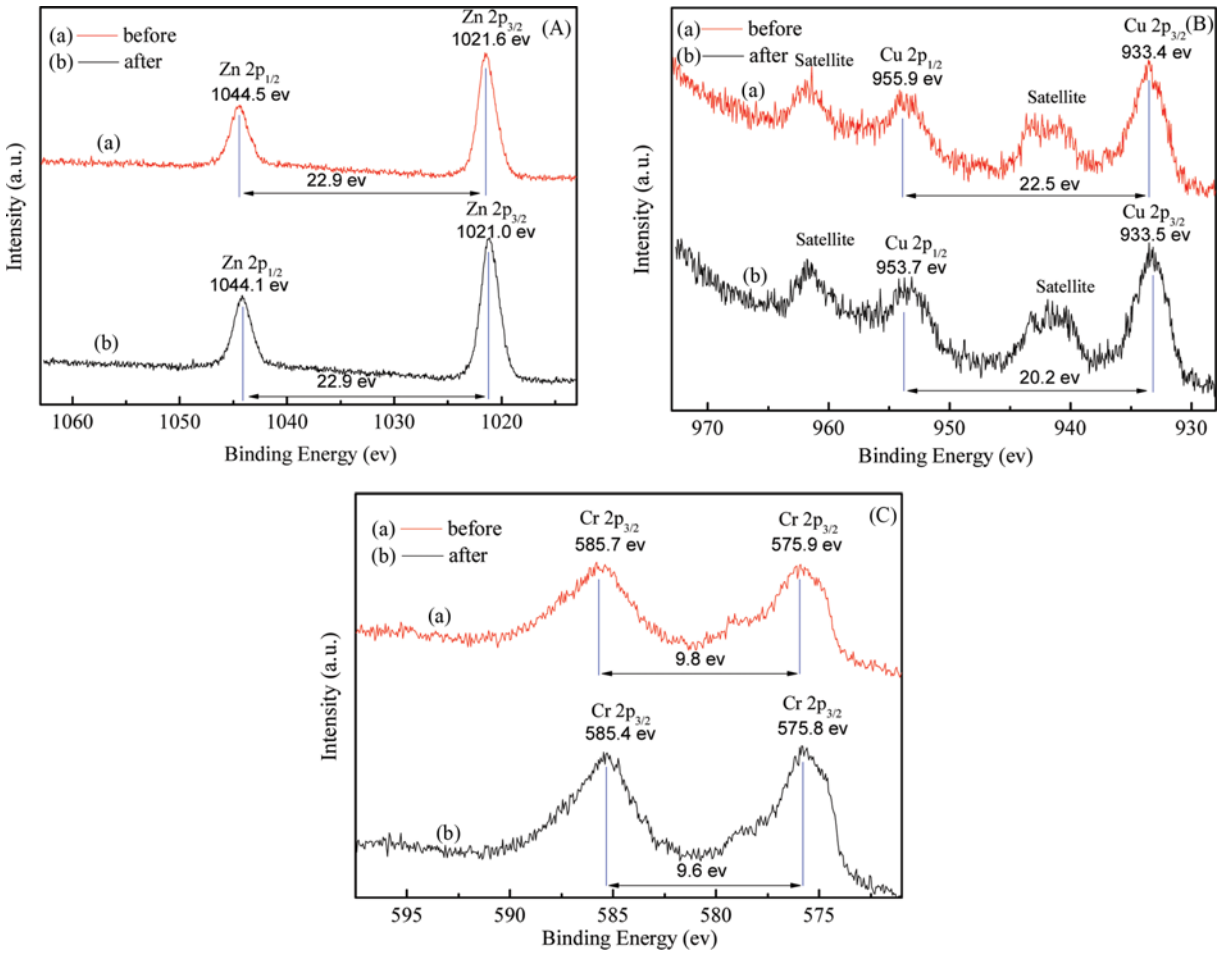

Fig. 5. XPS high-resolution spectra of the metallic elements in ZnSBCuCr-MO before and after photocatalytic degradation.

to Cu 2p3/2 and Cu 2p1/2. Meanwhile, the shakeup satellite peaks around 943 eV and 961 eV due to the satellite, which is the characteristic of CuO, also appear in Fig. 5(B-a). The difference of 22.5 eV in Cu 2p3/2 and Cu 2p1/2 levels and the emergence of satellite peaks indicate an oxidation state of 2+ for the Cu element [26]. As shown in Fig. 5(C-a), the binding energies of 575.9 eV and 585.7 eV are ascribed to Cr 2p3/2 and Cr 2p1/2. The difference of 9.8 eV in Cr 2p3/2 and Cr 2p1/2 levels indicates an oxidation state of 3+ for the Cr element [27]. For ZnSBCuCr-MO after photocatalytic degradation, the high resolution spectra of Zn2p, Cu2p, and Cr2p are shown in Fig. 5(A-b), Fig. 5(B-b), and Fig. 5(C-b), respectively. Compared with the XPS spectra of ZnSBCuCr-MO before photocatalytic degradation the variations of the peaks of Zn2p, Cu2p, and Cr2p doublet are negligible. Therefore, it is clear that the oxidation states of the metallic elements are retained after photocatalytic degradation suggesting that ZnSBCuCr-MO is stable.

2. Photocatalytic Activities of the Prepared Materials

The photocatalytic activities of the three materials were investigated by the degradation of RhB. As shown in Fig. 6, the photocatalytic degradation efficiency of ZnSBCuCr-MO reached over 90%, while that of ZnCr-MO and ZnCuCr-MO was only 57% and 75%. At the same time, the results of XRD also showed that CuO with narrower band gap was introduced into ZnSBCuCr-MO to modify the original composite of ZnO, Cr_2O_3 and $ZnCr_2O_4$. It would further promote the separation of photo-generated electrons and holes and improve the material's photocatalytic activity [28-30]. To

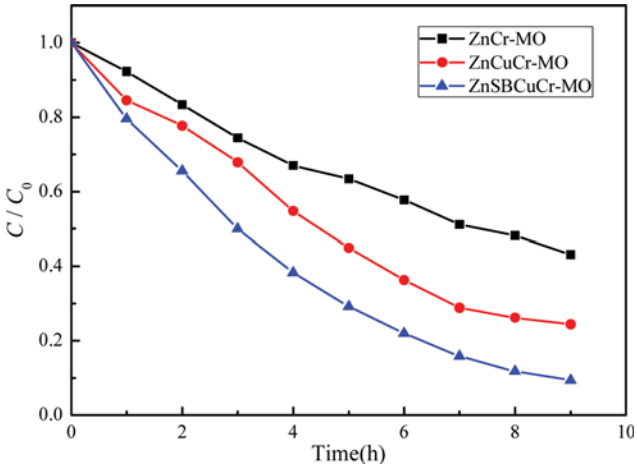

Fig. 6. Photocatalytic degradation of RhB by different materials (RhB concentration: 5 mg/L; material dosage: 1 g/L; pH: 7.40; temperature: 25 °C).

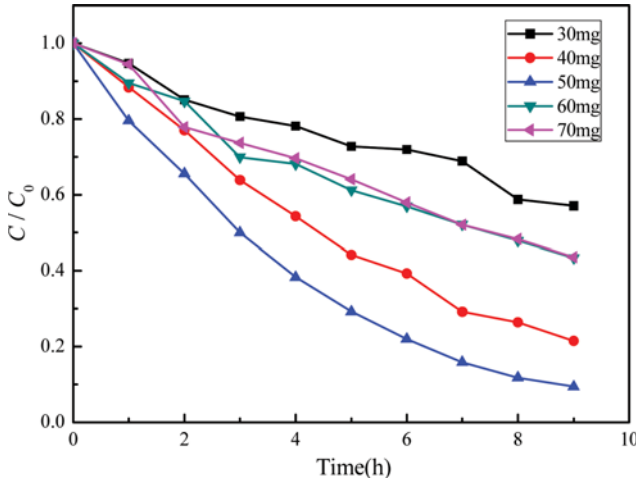

Fig. 7. Influence of ZnSBCuCr-MO dosage on RhB degradation (RhB concentration: 5 mg/L; pH: 7.40; temperature: 25 °C).

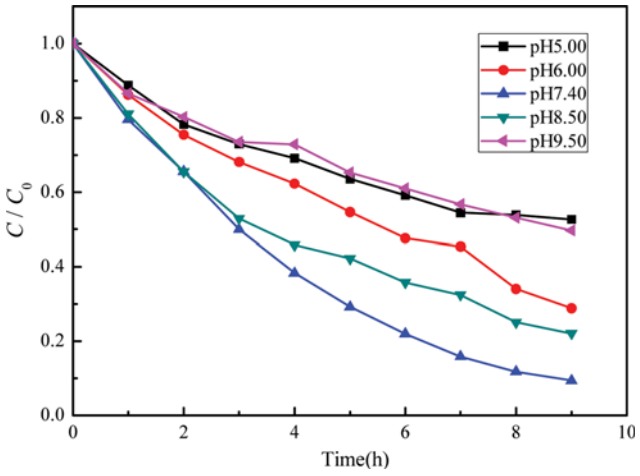

Fig. 8. Influence of initial pH on RhB photodegradation by ZnSBCuCr-MO (RhB concentration: 5 mg/L; material dosage: 1 g/L; temperature: 25 °C).

obtain maximum photocatalytic degradation efficiency with ZnSBCuCr-MO, the influence of catalytic material's dosage, the pH of dye, and the reaction temperature were studied.

2-1. Influence of Photocatalytic Material Dosage

To avoid excessive use of photocatalytic material and to find the optimum dosage of photocatalytic material for optimal photocatalytic efficiency, the effect of ZnSBCuCr-MO dosage ranged in 30-70 mg on photocatalytic degradation of RhB was investigated. As shown in Fig. 7, at the beginning, the degradation efficiency of RhB increased with the increasing of the photocatalytic material. The degradation efficiency of RhB increased from 43% to 91% with the dosage of photocatalytic material increased from 30 mg to 50 mg. While, with the continuous increasing dosage of photocatalytic material, the degradation efficiency of RhB decreased. The main reason was that the increase of the material's dosage would increase the number of active sites on the material surface. Thus, the number of photons adsorbed and the amount of RhB molecules adsorbed increased, resulting in an increase of degradation efficiency. On the other hand, since the catalytic material was insoluble in the reaction system, a continuous increase in the amount of the material caused an increase in the light scattering and a decrease in the light transmittance of the solution. This led to a reduction in the number of effective catalytic material particles and a decrease in the degradation efficiency of RhB.

2-2. Influence of Initial pH of RhB Solution

At present, the wastewater discharged from chemical plant, printing and dyeing factory, pharmaceutical factory and so on has large pH range. So, the pH of RhB solution is also an important variable affecting photocatalytic degradation. In the study of initial pH influence, the pH of RhB solution was adjusted in the range of 5.0-9.5, using 0.01 M HCl and NaOH. As shown Fig. 8, the best photocatalytic activity of ZnSBCuCr-MO was achieved at pH=7.40, while the photocatalytic activity decreased after changing the initial pH value. As the pH value of the solution increased, the positive charge on the surface of the material decreased and the negative charge increased, which enhanced the adsorption of cationic dye RhB and promoted the photocatalytic reaction. But, too high pH

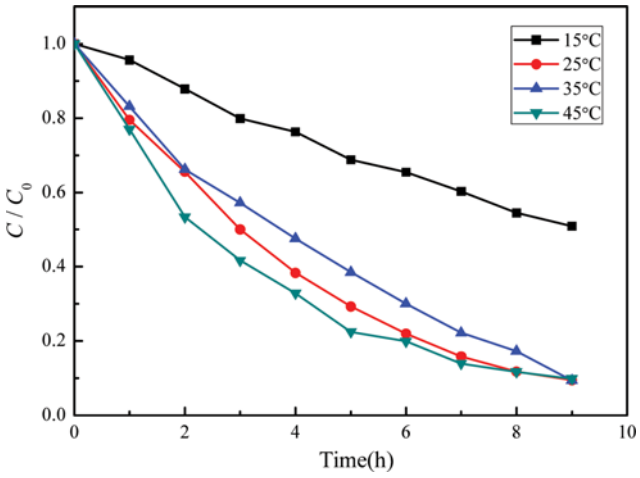

Fig. 9. Influence of reaction temperature on RhB photodegradation by ZnSBCuCr-MO (RhB concentration: 5 mg/L; material dosage: 1 g/L; pH: 7.40).

value may cause the destruction of the catalytic material and the competitive adsorption of Na^+ and RhB cations, leading to a reduction in the RhB adsorbed on the composite surface [31].

2-3. Influence of Reaction Temperature

Reaction temperature is another operational parameter affecting the photocatalytic efficiency. As shown in Fig. 9, the degradation efficiency of RhB increased with the increase of solution temperature. It was determined that the increase of the reaction temperature would promote the movement of the dye molecules more intensely, making the dye molecules more easily penetrate into the microvoids of the material. In addition, at higher temperatures, the movement of the photoelectron-hole pair became more active. Then, the electrons could combine with the adsorbed oxygens more quickly, and the holes can more quickly generated OH radicals with -OH, thereby improving the degradation efficiency of RhB. On the other hand, when the reaction temperature continued to rise, the degradation efficiency of RhB reached equilibrium. It

indicated that the reaction temperature had little effect on the photocatalytic activity when it rose to a certain value. Therefore, the optimum temperature of the reaction solution can be selected to be 25 °C for economic reasons.

2-4. Regeneration of the Materials

The effective reuse of photocatalytic materials is important in practical applications. However, some traditional photocatalytic materials (such as some TiO_2 based materials) are restricted in practical application due to the disadvantages of difficult separation and reclaim [11,12]. Hence, the photocatalytic activity of the regenerated ZnSBCuCr-MO was investigated and compared with the traditional calcined LDHs (ZnCr-MO and ZnCuCr-MO). Here, three successive photodegradations were performed under the same conditions. After each treatment, the materials were centrifugally separated, washed with deionized water, and dried at 65 °C. Fig. 10 presents the photodegradation results of the three successive cycles of the materials. After three photocatalytic cycles, the decreasing efficiency of RhB degradation by ZnSBCuCr-MO was only 10%, which was lower than that of the traditional calcined LDHs (ZnCr-MO and ZnCuCr-MO). Therefore, ZnSBCuCr-MO will be a potential photocatalyst with good performance and high reusability.

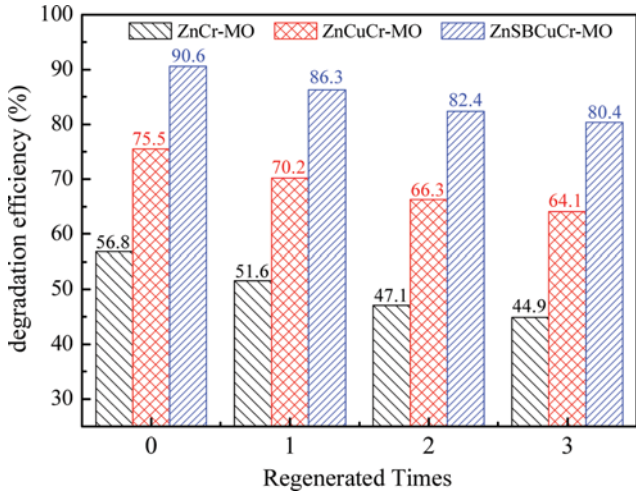

Fig. 10. Regeneration of ZnSBCuCr-MO, ZnCr-MO and ZnCuCr-MO.

3. Preliminary Study on the Mechanism and Path of Photocatalytic Degradation

Generally speaking, in the process of photocatalytic degradation, direct oxidation of the hole and the oxidation-reduction reaction of active radicals (•OH) are considered to be the main mechanism [32,33]. But, there is no unified understanding of the mechanism and the path of photodegradation of RhB [34-36]. So, we studied from the perspective of combining theory with experiment. The reaction sites were predicted by theoretical calculations of the frontier electron density (FEDs) of RhB molecule, and the possible degradation pathways were deduced by UV-vis absorption variation analysis and LC-MS analysis in the degradation process.

First, the frontier electron density (FEDs) of RhB molecule was calculated based on density functional theory (DFT). The energy structure of each atom in RhB was calculated accurately by the Dmol3 program module using Materials Studio 5.5 software and the results are shown in Table 2. According to frontier orbital theory, electrons can be easily lost at the sites with higher $2FED^2_{HOMO}$ value, while the sites with higher $FED^2_{HOMO}+FED^2_{LUMO}$ value are more likely to be attacked by •OH radicals [37-39]. From the data in the Table 2, N21 and N26 have the highest $2FED^2_{HOMO}$ value. Thus, N21 and N26 were likely the main initial positions for direct hole oxidation of RhB, resulting in the loss of electrons to produce a deethylation reaction. On the other hand, C1 had the highest $FED^2_{HOMO}+FED^2_{LUMO}$ value. So, C1 was most likely to be attacked by a •OH radical to generate 2-hydroxybenzoic acid and N-(6-(diethylamino)-3H-xanthen-3-ylidene)-N-ethylethanaminium [40].

Table 2. Frontier electron densities on atoms of RhB calculated by DFT analysis

Atom (no.)	$2FED^2_{HOMO}$	$FED^2_{HOMO}+FED^2_{LUMO}$	Atom (no.)	$2FED^2_{HOMO}$	$FED^2_{HOMO}+FED^2_{LUMO}$
C1	0.0012	**0.3412**	C18	0.0003	0.0414
C2	0.2008	0.1155	C19	0.0006	0.0286
C3	0.0089	0.0603	C20	0.0010	0.0315
O4	0.0021	0.0820	**N21**	**0.4097**	0.2739
C5	0.0187	0.0742	C22	0.0053	0.0053
C6	0.1757	0.1003	C23	0.0457	0.0312
C7	0.0062	0.0801	C24	0.0036	0.0035
C8	0.1182	0.0853	C25	0.0052	0.0040
C9	0.0462	0.1015	**N26**	**0.5726**	0.3502
C10	0.0742	0.0385	C27	0.0051	0.0053
C11	0.1416	0.0722	C28	0.0072	0.0044
C12	0.0576	0.1049	C29	0.0076	0.0065
C13	0.1191	0.0851	C30	0.0640	0.0409
C14	0.0160	0.0865	C31	0.0007	0.0183
C15	0.0009	0.0270	O32	0.0085	0.0278
C16	0.0002	0.0694	O33	0.0016	0.0101
C17	0.0004	0.0085			

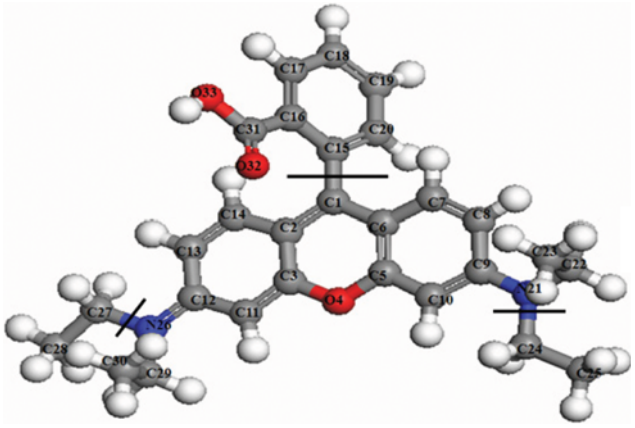

Fig. 11. The Structure of RhB.

The specific cleavage positions are indicated in the molecular structure diagram of RhB (Fig. 11).

Then, the RhB solution was made a absorption spectrum scan in the range of 450-650 nm wavelength at 0 h, 1 h, 3 h, 6 h, and 9 h during photocatalytic reaction. Fig. S1 shows the absorption variation during the photocatalytic degradation process of RhB over ZnSBCuCr-MO under visible light radiation. It was obvious that the maximum absorption of RhB decreased gradually as the photocatalytic reaction proceeded indicating that RhB was degraded due to the cleavage of the chromophore structure. Furthermore, the maximum absorption of degraded RhB exhibited blue shifts (554 nm-546 nm). It was probably because a series of deethylation reactions took place during the photocatalytic degradation process of RhB [41].

To confirm the results of theoretical calculation and UV-vis absorption variation analysis, the RhB solution after 4 h of photocatalytic reaction was analyzed by LC-MS to find the corresponding debris molecules (Fig. S2-S7 in supplementary data). In the reaction system, the main-intermediates were undegraded RhB (m/z=443, RT=5.9 min), products of removal of some ethyl groups from N21 and N26 (m/z=415, RT=4.3 min, m/z=387, RT=3.4 min), and products of further degradation of N-(6-(diethylamino)-3H-xanthen-3-ylidene)-N-ethylethanaminium (m/z=282, 252, RT=

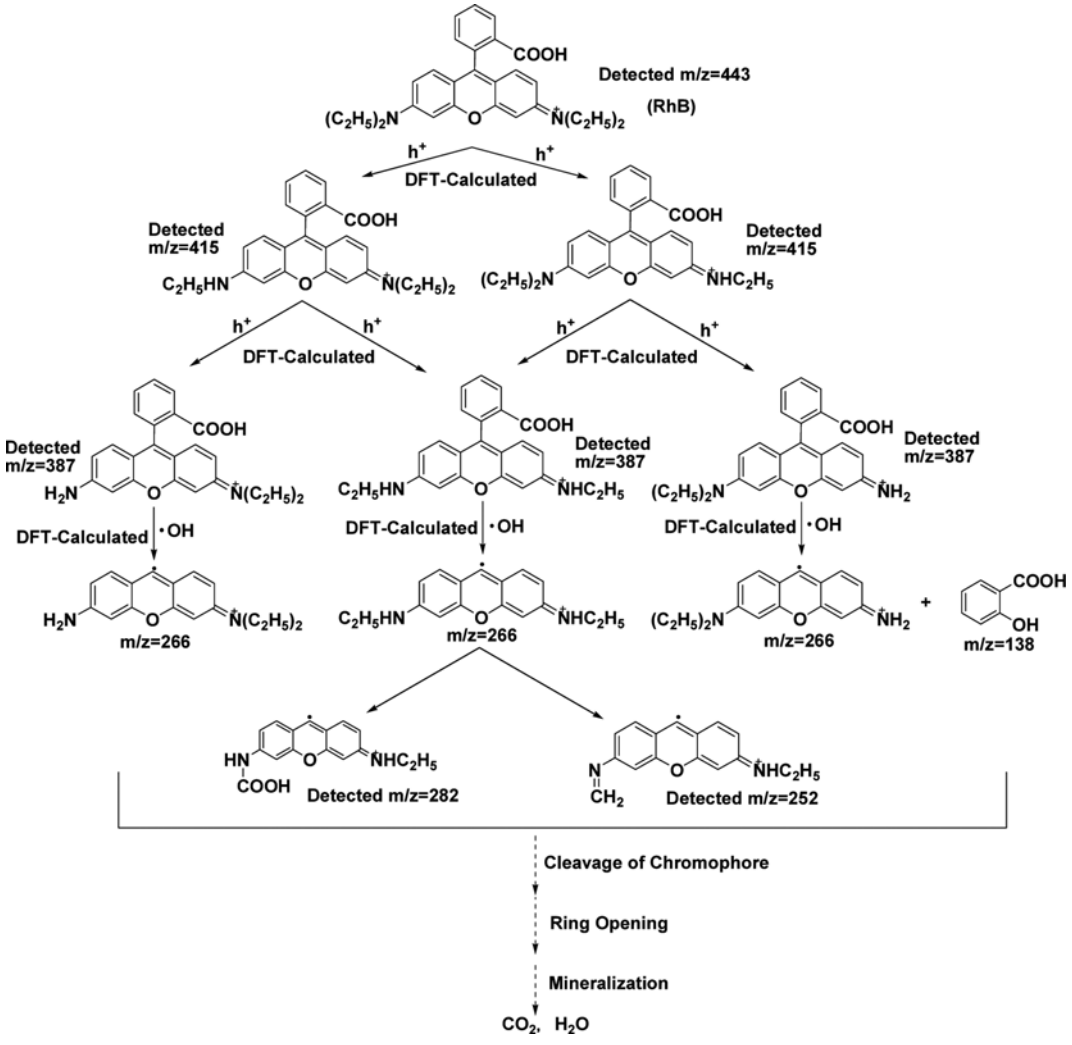

Scheme 3. The possible mechanism and pathway for photocatalytic degradation of RhB.

3.5 min, 4.0 min). The above results are in good agreement with the predicted photocatalytic degradation mechanism by DFT theoretical calculation and UV-vis absorption variation analysis.

Therefore, according to the DFT theoretical of FEDs calculation, UV-vis absorption variation analysis and LC-MS analysis, the possible mechanism and path of photocatalytic degradation of RhB are shown in Scheme 3.

CONCLUSION

ZnSBCuCr-MO derived from Salen-Cu(II) intercalated ZnCr-LDHs was successfully synthesized by coprecipitation and calcination. ZnSBCuCr-MO composed of narrow-band gap semiconductor (CuO) and wide-band gap semiconductors (ZnO, Cr_2O_3 and $ZnCr_2O_4$) had the advantages of small band gap and large visible-light response range exhibiting excellent photocatalytic performance. Under the optimal experimental condition of 25 °C, pH 7.4, 5 mg/L of RhB solution and 1 g/L ZnSBCuCr-MO, the degradation efficiency of RhB was 91%, compared to 57%, 75% by ZnCr-MO and ZnCuCr-MO, respectively. And, ZnSBCuCr-MO also exhibited stronger stability and better reusability. In addition, the mechanism and path of photocatalytic degradation of RhB were predicted by the DFT theory calculation based on FEDs, UV-vis absorption variation analysis and LC-MS analysis. It was found that the photocatalytic degradation of RhB occurred mainly through de-ethylation reactions of direct holes (+) oxidation and oxidation-reduction reactions involved with •OH radicals.

ACKNOWLEDGEMENTS

This work was financed by the National Natural Science Foundation of China (21503188) and the Zhejiang Provincial Natural Science Foundation of China (LQ15B030002).

SUPPORTING INFORMATION

Additional information as noted in the text. This information is available via the Internet at http://www.springer.com/chemistry/journal/11814.

REFERENCES

1. S. Alessia, G. C. Antonio, A. D. Melissa, M. Stefan, P. Massimo, S. Anna, T. Roberto and V. Antonio, *J. Hazard. Mater.*, **300**, 504 (2015).
2. N. Baliarsingh, L. Mohapatra and K. Parida, *J. Mater. Chem. A.*, **1**, 4236 (2013).
3. G. X. Pan, X. H. Xia, J. S. Luo, F. Cao, Z. H. Yang and H. J. Fan, *Appl. Clay Sci.*, **102**, 28 (2014).
4. M. N. Timofeeva, A. E. Kapustin, V. N. Panchenko, E. O. Butenko, V. V. Krupskaya, A. Gil and M. A. Vicente, *J. Mol. Catal. A: Chem.*, **423**, 22 (2016).
5. S. Xu, J. Y. Yu, Y. B. Sun and S. P. Wu, *Mater. Chemi. Phys.*, **152**, 54 (2015).
6. Y. M. Shen, X. L. Zhao, X. Zhang, S. F. Li, D. B Liu and L. H. Fan, *Korean J. Chem. Eng.*, **33**, 159 (2016).
7. S. Singha, M. Sahoo and K. M. Parida, *Dalton T.*, **40**, 11838 (2011).
8. Y. L. Wang, P. X. Wu, Y. K. Hou, N. W. Zhu and Z. Dang, *Ind. Eng. Chemi. Res.*, **51**, 11128 (2012).
9. K. M. Parida, N. Baliarsingh, B. S. Patra and J. Das, *J. Mol. Catal. A: Chem.*, **267**, 202 (2007).
10. J. Schneider, M. Matsuoka, M. Takeuchi, J. l. Zhang, Y. Horiuchi, M. Anpo and D. W. Bahnemann, *Chem. Rev.*, **114**, 9919 (2014).
11. J. G. Yu, S. H. Wang, J. X. Low and W. Xiao, *Phys. Chem. Chem. Phys.*, **15**, 16883 (2013).
12. K. Yasui, T. Isobe and A. Nakajima, *Mater. Lett.*, **64**, 2036 (2010).
13. L. H. Zhang, Z. G. Xiong, L. Li, R. Burt and X. S. Zhao, *J. Colloid Interface Sci.*, **469**, 224 (2016).
14. C. Alanis, R. Natividad, C. Barrera-Diaz, V. Martínez-Miranda, J. Prince and J. S. Valente, *Appl. Catal. B: Environ.*, **140-141**, 546 (2013).
15. X. X. Tang, Y. Liu and S. H. Li, *RSC Adv.*, **6**, 80501 (2016).
16. N. Y. Lu, B. J. Li, B. B. Fan, W. Y. Guo and R. F. Li, *Mater. Chem. Phys.*, **167**, 219 (2015).
17. G. Varga, Á. Kukovecz, Z. Kónya, L. Korecz, S. Muráth, Z. Csendes, G. Peintler, S. Carlson, P. Sipos and I. Pálinkó, *J. Catal.*, **335**, 125 (2016).
18. L. J. Zhang, Y. C. Chen, Z. M. Zhang and C. Lu, *Sensor. Actuat. B: Chem.*, **193**, 752 (2014).
19. S. J. Xia, Y. Meng, X. B. Zhou, J. L. Xue, G. X. Pan and Z. M. Ni, *Appl. Catal. B: Environ.*, **187**, 122 (2016).
20. S. J. Xia, L. Y. Zhang, X. B. Zhou, M. M. Shao, G. X. Pan and Z. M. Ni, *Appl. Catal. B: Environ.*, **266**, 176 (2015).
21. L. G. Yan, K. Yang, R. R. Shan, T. Yan, J. Wei, S. J. Yu, H. Q. Yu and B. Du, *J. Colloid Interface Sci.*, **448**, 508 (2015).
22. M. J. Li, Z. B. Yu, Q. Liu, L. Sun and W. Y. Huang, *Chemi. Eng. J.*, **286**, 232 (2016).
23. S. J. Xia, L. Y. Zhang, G. X. Pan, P. P. Qian and Z. M. Ni, *Phys. Chem. Chem. Phys.*, **17**, 5345 (2015).
24. B. M. Pirzada, N. A. Mir, N. Qutub, O. Mehraj, S. Sabir and M. Muneer, *Mater. Sci. Eng. B.*, **193**, 137 (2015).
25. H. P. Li, Q. H. Deng, J. Y. Liu, W. G. Hou, N. Du, R. J. Zhang and X. T. Tao, *Catal. Sci. Technol.*, **4**, 1028 (2014).
26. F. Li, Y. Yin and D. M. Jiang, *J. Mater. Sci.*, **52**, 6415 (2017).
27. A. Hastir, N. Kohli, O. S. Kang and R. C. Singh, *J. Electroceram.*, **37**, 170 (2016).
28. R. Lamba, A. Umar, S. K. Mehta and S. K. Kansal, *Alloys Compd.*, **653**, 327 (2015).
29. J. Luo, X. S. Zhou, L. Ma and X. Y. Xu, *J. Mol. Catal. A: Chem.*, **410**, 168 (2015).
30. S. Khanchandani, S. Kundu, A. Patra and A. K. Ganguli, *J. Phys. Chem. C.*, **117**, 5558 (2013).
31. S. B. Wang and Z. H. Zhu, *Dyes Pigm.*, **75**, 306 (2007).
32. Z. H. Zhang, S. Y. Zhai, M. H. Wang, H. F. Ji, L. H. He, C. M. Ye, C. B. Wang, S. M. Fang and H. Z. Zhang, *J. Alloys Compd.*, **659**, 101 (2016).
33. L. X. Hu, F. Y. Chen, P. F. Hu, L. P. Zou and X. Hu, *J. Mol. Catal. A: Chem.*, **411**, 203 (2016).
34. J. M. Fang, X. Y. Huang, Q. Zhang, J. Chen and X. Wang, *Appl. Surf. Sci.*, **360**, 994 (2016).
35. X. X. Yang, C. D. Cao, L. Erickson, K. Hohn, R. Maghirang and K. Klabunde, *Appl. Catal. B: Environ.*, **91**, 657 (2009).

36. G. X. Chen, S. M. Qian, X. M. Tu, X. Y. Wei, J. P. Zou, L. H. Leng and S. L. Luo, *Appl. Surf. Sci.*, **293**, 345 (2014).
37. N. Watanabe, S. Horikoshi, H. Kawabe, Y. Sugie, J. C. Zhao and H. Hidaka, *Chemosphere*, **52**, 851 (2013).
38. Y. Ohko, K. I. Iuchi, C. Niwa, T. Tatsuma, T. Nakashima, T. Lgu-chi, Y. Kubota and A. Fujishima, *Environ. Sci. Technol.*, **36**, 4175 (2002).
39. B. D. Lee, M. Iso and M. Hosomi, *Chemosphere*, **42**, 431 (2001).
40. T. C. An, H. Yang, G. Y. Li, W. H. Song, W. J. Cooper and X. P. Nie, *Appl. Catal. B-Environ.*, **94**, 288 (2010).
41. Z. He, C. Sun, S. G. Yang, Y. C. Ding, H. He and Z. L. Wang, *J. Hazard. Mater.*, **162**, 1477 (2009).

Supporting Information

Preparation and photocatalytic activity of composite metal oxides derived from Salen-Cu (II) intercalated layered double hydroxides

Yue Meng[*,], Shengjie Xia[*], Guoxiang Pan[***], Jilong Xue[*], Junhui Jiang[*], and Zheming Ni[*,†]**

*College of Chemical Engineering, Zhejiang University of Technology, Hangzhou 310014, China
**School of Life Sciences, Huzhou University, Huzhou 313000, China
***School of Engineering, Huzhou University, Huzhou 313000, China
(*Received 17 January 2017 • accepted 17 May 2017*)

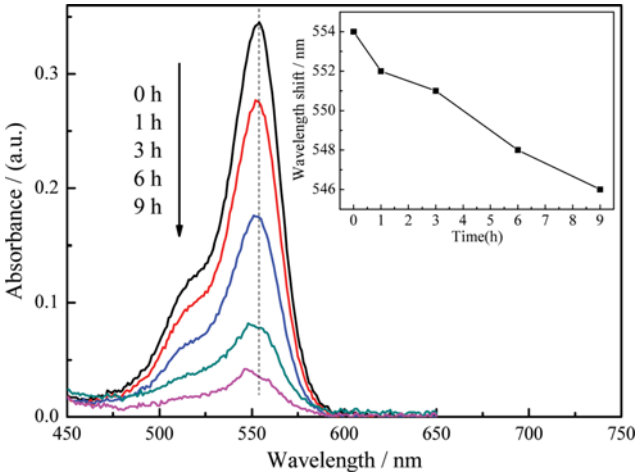

Fig. S1. Absorption changes of RhB and wavelength shifts of absorption maximum during the photodegradation process over ZnSBCuCr-MO.

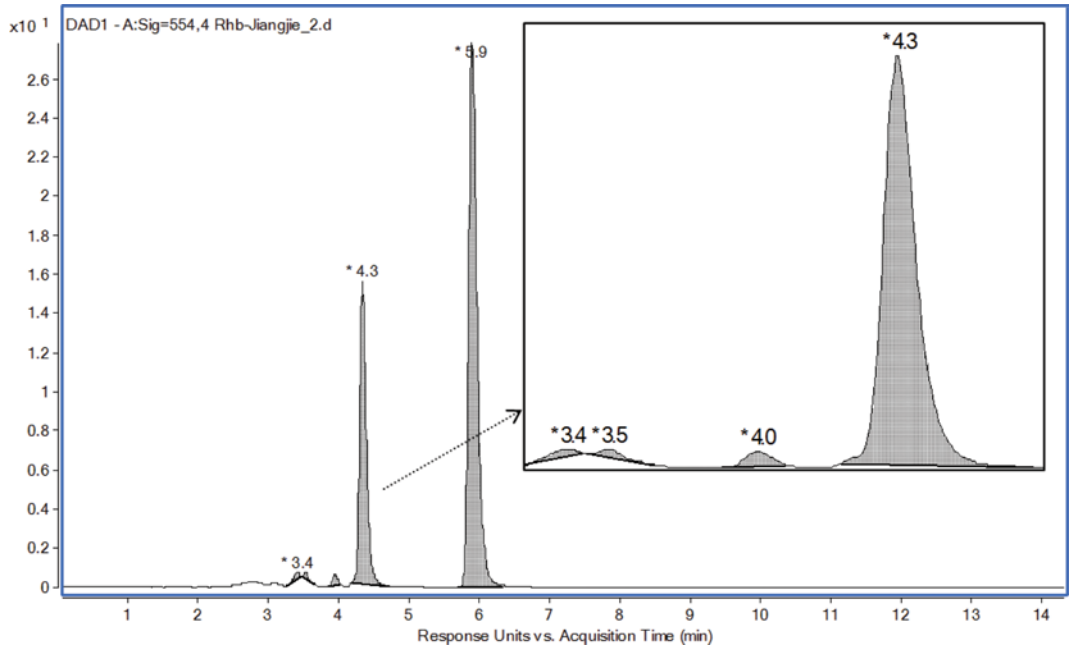

Fig. S2. The TIC chromatogram of rhodamin B solution after 4 h photo-degradation.

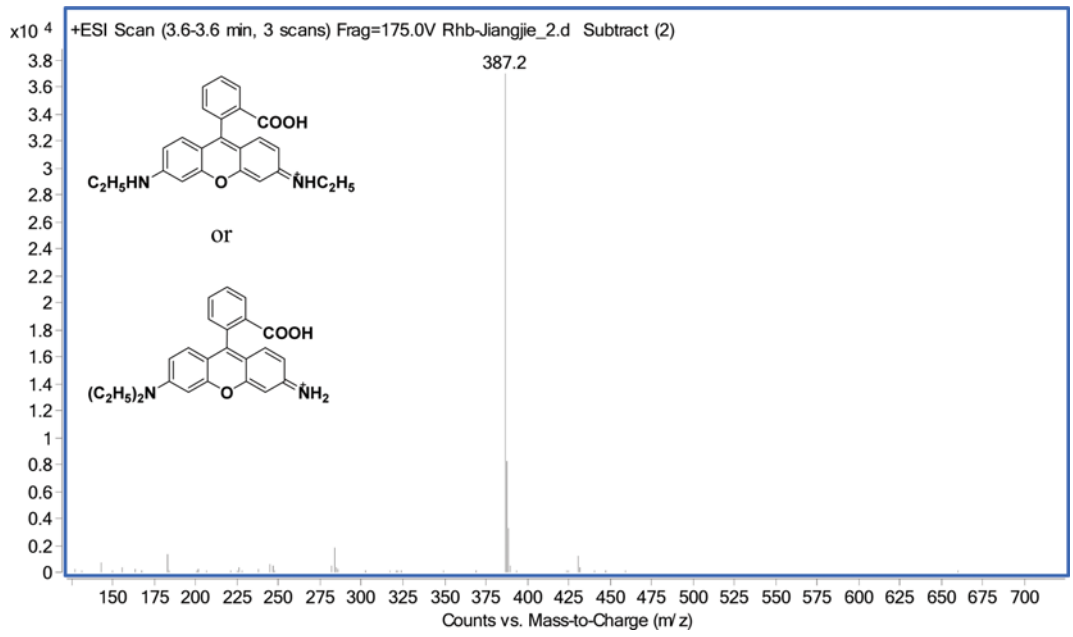

Fig. S3. ESI mass spectra of RhB degradation intermediate for RT=3.4 min.

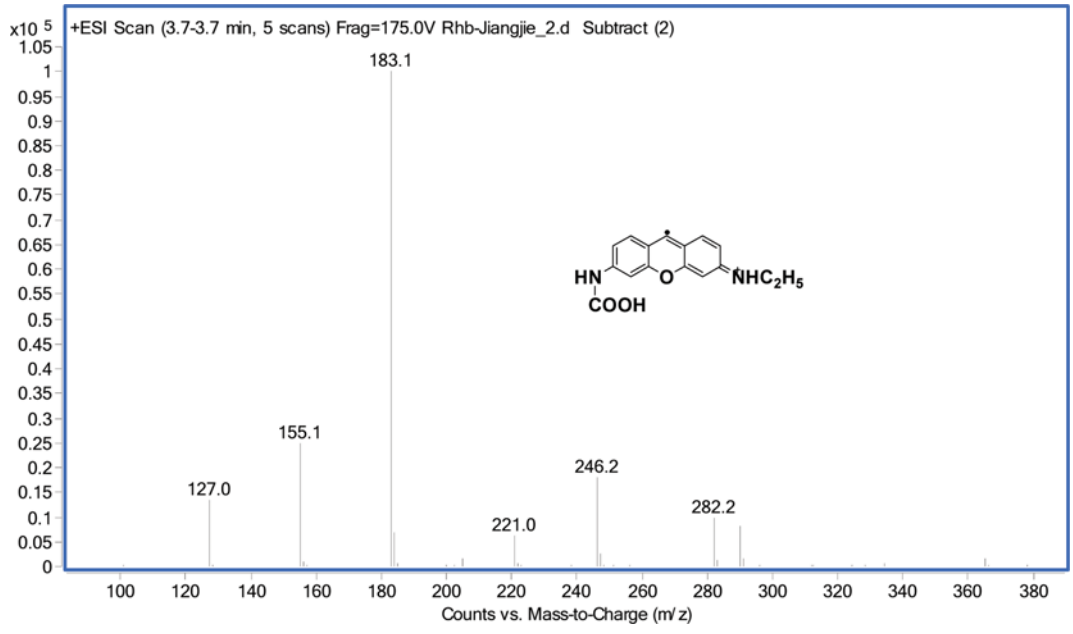

Fig. S4. ESI mass spectra of RhB degradation intermediate for RT=3.5 min.

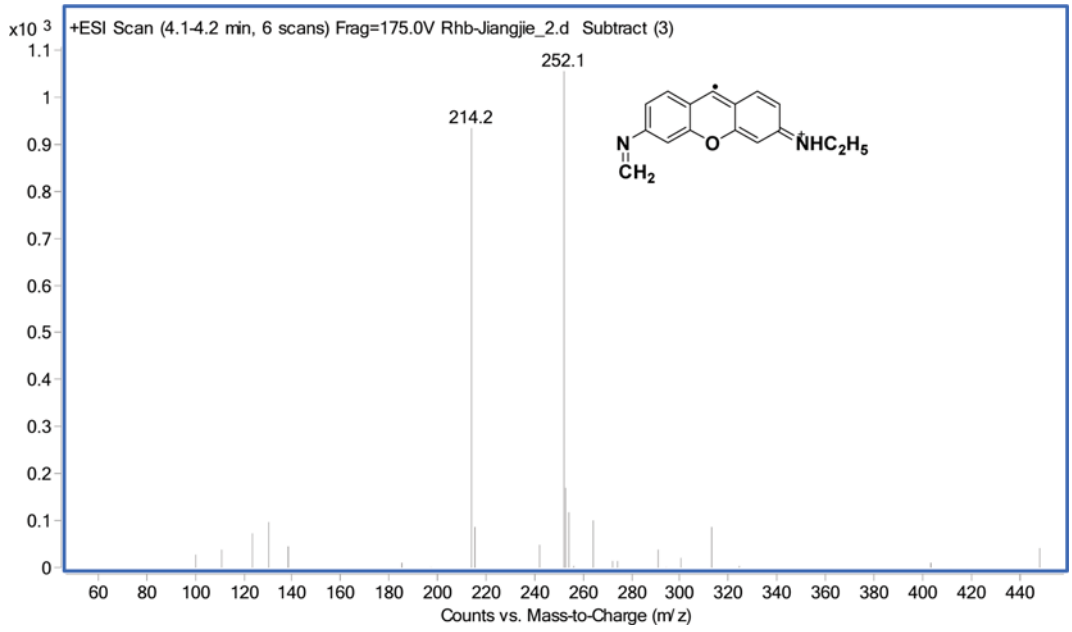

Fig. S5. ESI mass spectra of RhB degradation intermediate for RT=4.0 min.

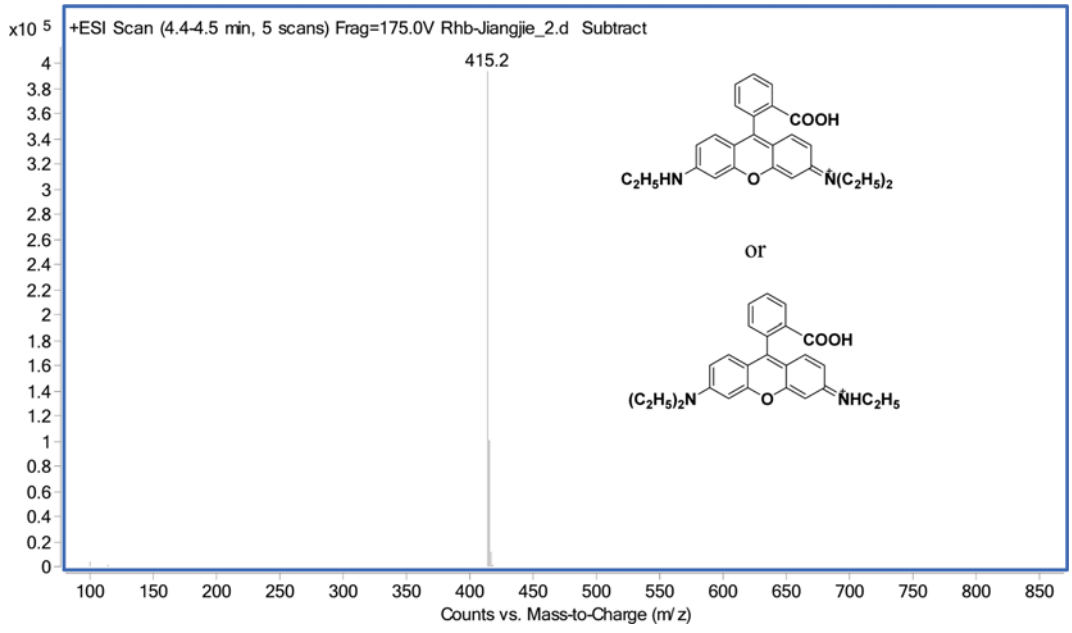

Fig. S6. ESI mass spectra of RhB degradation intermediate for RT=4.3 min.

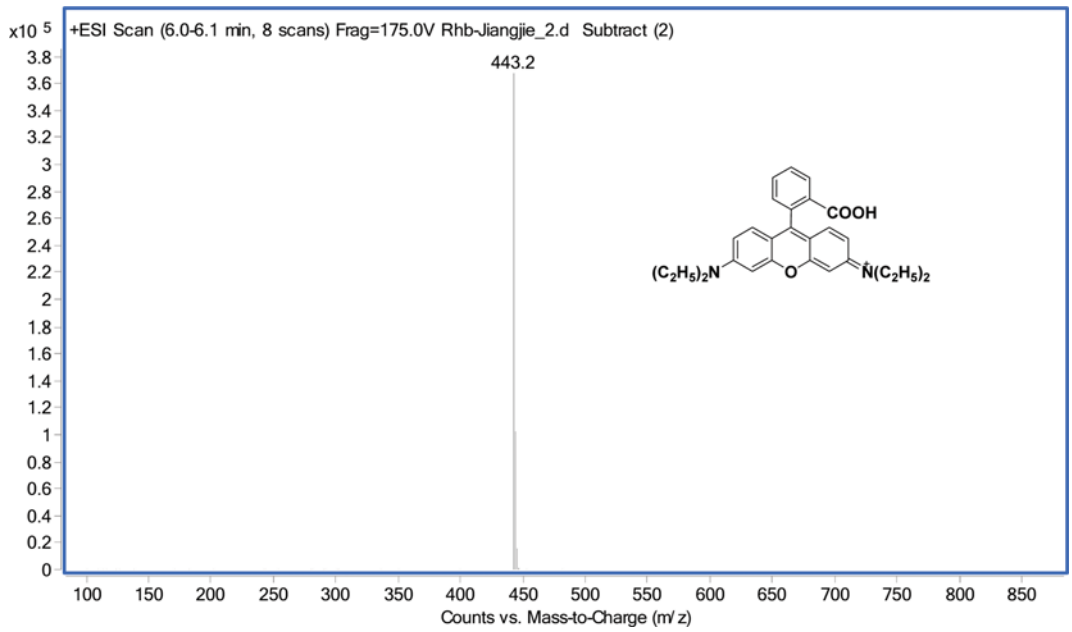

Fig. S7. ESI mass spectra of RhB degradation intermediate for RT=5.9 min.